

AEROELASTIC ANALYSIS OF AIRCRAFT WINGS

André S. Carneira[†], André C. Marta[‡]

CCTAE, IDMEC, Instituto Superior Técnico, Universidade de Lisboa
Av. Rovisco Pais 1, 1049-001 Lisboa, Portugal

[†] andre.carneira@tecnico.ulisboa.pt [‡] andre.marta@tecnico.ulisboa.pt

Keywords: Aeroelasticity, Panel method, Fluid-structure interaction, Finite element method, Flutter, Divergence velocity.

Abstract. *Aeroelasticity phenomena involve the study of the interaction between aerodynamic, inertial, and elastic forces (dynamic aeroelasticity). Modern aircraft structures, using more and more lightweight flexible composite materials, make the aeroelastic study an extremely important aspect in aircraft design. Flutter is a dynamic aeroelastic instability characterized by sustained oscillation of structure arising from interaction between those three forces acting on the body. The present work aims to study the flutter behavior on three-dimensional subsonic aircraft wings, using a computationally efficient method. For that, a computational aeroelasticity design framework is created using a custom developed panel method for the fluid flow analysis and a commercial software for the structural analysis. A validation of the flow solver is made using wind tunnel data, while the structural solver is verified using available tests. The coupling of the two domains is made using an adequate time discretization scheme. The results are presented for a reference wing. Following the wing baseline analysis, a parametric study under flutter conditions is performed, revealing some physically expected correlations: i) increasing the freestream velocity leads to higher vibration amplitude, whereas the frequency remains unchanged; ii) moving the wing spars aft or forward, causing the twist center to move away from the aerodynamic center, leads to instability; iii) decreasing the material density (weight) leads to higher flutter frequency and amplitude; iv) increasing the material stiffness (Young modulus) leads to higher frequency and smaller amplitude flutter. It is concluded that the framework shows very good agreement to the theoretical influences of the parameters studied. Despite the simplification of the fluid flow, which was assumed to be potential, this method proves to be a very useful tool in aircraft preliminary design.*

1 INTRODUCTION

Structural analyses constitute a crucial part in aircraft design. Since the primordials of the aviation history, it was stated that the success of the air vehicle is dependent on a structure capable of withstanding the several loads encountered in flight and a strong propulsion system. Moreover, both components should be as light as possible.

Aeroelastic phenomena in modern high-speed aircraft have profound upon the design of structural members and also upon mass distribution, lifting surface planforms and control system design [1]. Accurate computational aeroelastic tests can be applied in early stages of the design phase. By increasing the accuracy and feasibility of computational tools, one can decrease the number of experimental tests needed, which largely reduces the design costs. Also, applications of the aeroelastic phenomena are found in several other disciplines.

A general (but complete) definition is the one from [2]:

The science of aeroelasticity encompasses those physical processes and problems that result from the interaction between elasto-mechanical systems and the surrounding airflow.

To help visualizing the context of the term, a representation (firstly suggested in [11]) in triangle is used, presented in Figure 1.

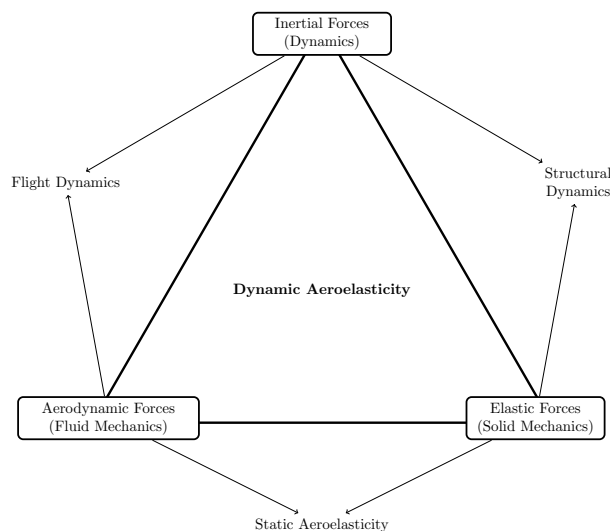


Figure 1: Collar triangle.

By pairing two of the three corners of the triangle, one can identify other important disciplines. For example,

- aerodynamics + dynamics = aerodynamic stability;
- dynamics + solid mechanics = structural dynamics;
- aerodynamics + solid mechanics = static aeroelasticity.

In some sense, all these technical fields may be considered special cases of aeroelasticity. However, for dynamic aeroelastic effects to occur, all three forces are required.

Flutter has perhaps the most far-reaching effects on high-speed aircraft [1]. The *classical* type of flutter is associated with potential flow and usually, involves coupling of two or more degrees of freedom (DOF). The *nonclassical* type of flutter may involve separated flow, turbulence and stalling conditions.

The object of study is the aircraft wing. The main structural parts are the spars, ribs, stringers and the skin (see Figure 2). Then, accordingly to the application, one can change their materials, quantity, location and geometry.

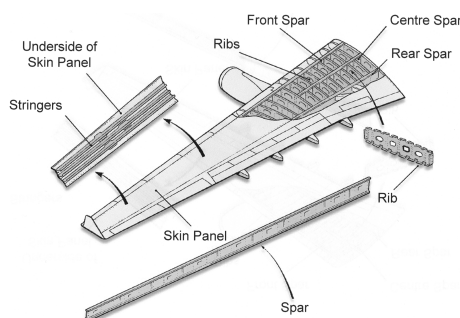


Figure 2: Illustration of the interior of an aircraft wing [8].

A simplified structure is used with only two spars and a skin. The skin will then be thicker to compensate the absence of stringers and the spars can be moved forward and backward to manipulate the torsional characteristics of the wing.

The objectives of this work are then to review the actual models and methods to compute aeroelastic calculations, state the governing equations and its acceptable approximations, and to apply some of these methods to perform aeroelastic studies of aircraft wings.

For these studies, an available tool for computational structural mechanics (CSM) analysis is employed, while the computational fluid dynamics (CFD) for aerodynamics and the coupling tools are to be created and merged in a computational program. The final result is an aeroelastic design framework for subsonic aircraft wings.

2 BACKGROUND

For the aeroelastic design framework, three domains of theory are treated: structural, fluid flow and fluid-structure coupling.

2.1 Structural Approach

The transient dynamic equilibrium equation is, for a linear structure,

$$M\ddot{\vec{u}} + C\dot{\vec{u}} + K\vec{u} = \vec{F}, \quad (1)$$

where M represents the structural mass matrix, C the structural damping matrix, K the structural stiffness matrix, $\ddot{\vec{u}}$ the nodal acceleration vector, $\dot{\vec{u}}$ the nodal velocity vector, \vec{u} the nodal displacement vector and \vec{F} the applied load vector.

In this work, the structural computations are made in the commercial software ANSYS Parametric Design Language (APDL). It has available two time integration schemes [3], being the most commonly used the implicit Newmark method, which applied to Equation (1) gives

$$\begin{aligned} \vec{u}_{n+1} (a_0 M + a_1 C + K) &= \vec{F} + \\ M \left(a_0 \vec{u}_n + a_2 \dot{\vec{u}}_n + a_3 \ddot{\vec{u}}_n \right) &+ , \\ C \left(a_1 \vec{u}_n + a_4 \dot{\vec{u}}_n + a_5 \ddot{\vec{u}}_n \right) & \end{aligned} \quad (2)$$

where

$$\begin{aligned} a_0 &= \frac{1}{\alpha \Delta t^2}, & a_1 &= \frac{\delta}{\alpha \Delta t}, \\ a_2 &= \frac{1}{\alpha \Delta t}, & a_3 &= \frac{1}{2\alpha} - 1, \\ a_4 &= \frac{\delta}{\alpha} - 1, & a_5 &= \frac{\Delta t}{2} \left(\frac{\delta}{\alpha} - 2 \right), \\ a_6 &= \Delta t (1 - \delta), & a_7 &= \delta \Delta t. \end{aligned}$$

As documented in [3], this scheme is unconditionally stable for

$$\alpha \geq \frac{1}{4} \left(\frac{1}{2} + \delta \right)^2, \quad \delta \geq \frac{1}{2}, \quad \frac{1}{2} + \delta + \alpha > 0, \quad (3)$$

where α and δ are the Newmark integration parameters and are related to the amplitude decay factor γ by $\alpha = \frac{1}{4}(1 + \gamma)^2$ and $\delta = \frac{1}{2} + \gamma$.

Three methods are available in APDL to solve Equation (2): the full, reduced and mode superposition. The full method simply solves Equation (2) with no additional assumptions, while the reduced forbids the use of pressure loads and the mode superposition has no element damping matrices. So, the full method is the one used for this task.

All the model will be constructed with SHELL181 elements. It is a four-node quadrilateral bi-linear element with six DOF at each node: translations in the x, y, and z directions and rotations about the x, y and z-axes.

2.2 Aerodynamic Approach

For the aerodynamic calculations, the *Potential Flow Model* is here applied. It is obtained assuming that the flow is inviscid, irrotational and isentropic. Compressible effects are out of the scope of this work, so the fluid is also assumed incompressible. With these assumptions, the governing equation is

$$\nabla \cdot \vec{V} = \nabla \cdot (\nabla \cdot \Phi) = \nabla^2 \Phi = 0, \quad (4)$$

where $\Phi(x, y, z)$ is the velocity potential. Equation (4) is a linear differential equation known as *Laplace* equation. It was extensively studied and it has many possible analytical solutions. Also, because it is linear, the *principle of superposition* applies. This means that if $\Phi_1, \Phi_2, \dots, \Phi_n$ are solutions of the Laplace equation, then

$$\Phi = \sum_{k=1}^n c_k \Phi_k \quad (5)$$

is also a solution for it (c_k are arbitrary constants).

The boundary conditions for this problem are the impermeability condition (zero normal velocity on a body) and the far field condition (the disturbance created by the motion should vanish far from the body).

The solutions in evidence here are the Source

$$\Phi = -\frac{\sigma}{4\pi |\vec{r} - \vec{r}_0|} \quad (6)$$

and the Doublet

$$\Phi = \frac{\mu}{4\pi} \frac{\partial}{\partial n} \frac{1}{|\vec{r} - \vec{r}_0|}, \quad (7)$$

where σ and ν are the source and doublet strength, respectively.

The pressure computation is made using the *Bernoulli* equation for inviscid incompressible irrotational flow,

$$E + \frac{p}{\rho} + \frac{V^2}{2} + \frac{\partial \Phi}{\partial t} = C(t), \quad (8)$$

where E is the gravitational potential, p pressure, ρ density and V velocity. This means that at a certain time t_1 , the quantity at the left-hand side of Equation (8) must be equal throughout the field. Particularly, one can compare any point of the field with a reference point. If this reference condition is chosen such that $E = 0$ (no body forces) and $\Phi_\infty = const.$, then the pressure coefficient C_p at any point can be calculated from

$$C_p = \frac{p - p_\infty}{0.5\rho V_\infty^2} = 1 - \frac{V^2}{V_\infty^2} - \frac{2}{V_\infty^2} \frac{\partial \Phi}{\partial t}, \quad (9)$$

where the subscript ∞ denotes far-field conditions. The integration over time demands a time discretization method. Since the goal is to obtain the pressure coefficient at the time $t + \Delta t$, an implicit method is required. The simpler and still largely used option is the *Backward Euler* method [4], which applied to Equation (9) yields

$$C_p^{t+\Delta t} = 1 - \frac{(V^{t+\Delta t})^2}{V_\infty^2} - \frac{2}{V_\infty^2} \left(\frac{\Phi^{t+\Delta t} - \Phi^t}{\Delta t} \right), \quad (10)$$

which is first order accurate. A second order accurate possibility is the *Crank-Nicholson* method [4].

From here, a panel method was built based on the formulation from [5] using constant quadrilateral sources and doublets. The Dirichlet boundary condition results in the form

$$\begin{aligned} & \frac{1}{4\pi} \int_{body+wake} \mu \vec{n} \cdot \nabla \left(\frac{1}{r} \right) dS - \\ & \frac{1}{4\pi} \int_{body} \sigma \left(\frac{1}{r} \right) dS = 0 \end{aligned} \quad (11)$$

The body surface is now discretized into N surface panels and the wake is modeled using N_W panels. This problem is then reduced to a set of linear algebraic equations

$$\sum_{k=1}^N C_k \mu_k + \sum_{l=1}^{N_W} C_l \mu_l + \sum_{k=1}^N B_k \sigma_k = 0, \quad (12)$$

where for each collocation point the summation of the influences of all k body panels and l wake panels is needed. Since the singularity elements have constant strength in each panel, the integrals depend only on the geometry.

For Equation (11) to be valid and from the definition of the source strength σ , it comes an additional condition that

$$\sigma = \vec{n} \cdot \vec{V}_\infty. \quad (13)$$

This way, the third term in Equation (12) is calculated and can be moved to the right-hand side.

The influence from the wake comes from the linear Kutta condition

$$\mu_W = \mu_U - \mu_L, \quad (14)$$

where μ_U and μ_L are the upper and lower surface doublet strengths at the trailing edge and μ_W is constant along the wake (in a steady problem).

In an unsteady case, the wake shape is obtained using a time-stepping method. Herein the wake is directly related to the motion, being convected with \vec{V}_∞ at each time step.

2.3 Fluid-Structure Coupling

The coupling between fluid and structural domains is normally referred as *Fluid-Structure Interaction* (FSI). The range of FSI models can be divided in two categories: strongly-coupled (or monolithic) and loosely-coupled (or staggered). A monolithic approach would be for this case, to merge Equations (1) and (9) and to integrate over time.

The other option is a staggered procedure. For a given time step, such an algorithm typically involves the solution of the fluid mechanics with the velocity boundary conditions coming from the previous step, followed by the solution of the structural mechanics equations with the updated fluid interface load, and followed by the mesh movement with the new structure displacement. The basic algorithm is the so called *Conventional Serial*

Staggered (CSS) procedure [6]. It is graphically depicted in Figure 3, where \vec{U} denotes the structure state vector (nodal displacement and velocity), \vec{W} denotes the fluid state vector (in the case of a complete fluid discretization), \vec{p} designates the fluid pressure, n stands for the n^{th} time station, and the equalities shown at the top hold on the fluid/structure interface boundary.

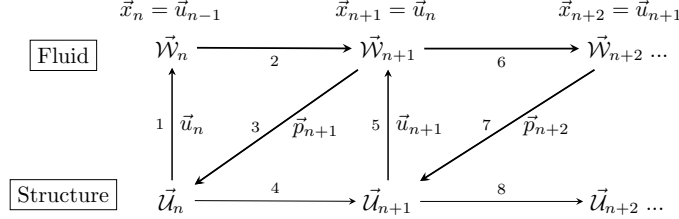


Figure 3: The Conventional Serial Staggered (CSS) scheme.

A similar procedure was also presented in [6], the *Improved Serial Staggered (ISS)*, which uses the structural velocity and calculates the fluid states at the middle of each time step.

3 IMPLEMENTATION

First, some verification tests were made using APDL Verification Manual. Then, an aircraft wing was used to make a mesh convergence test, using four different meshes: 16×10 , 32×20 , 64×40 and 128×80 . These numbers represent the number of panels of the skin in the form *chordwise* \times *spanwise*.

The wing has NACA 0010 airfoil and an aspect ratio $\mathcal{R} = 4$. Two spars are introduced inside the skin at 30% and 70% chord distance from the leading edge (Figure 4). The material used has Young modulus $E = 200 \text{ GPa}$, Poisson ratio $\nu = 0.3$ and thickness of 10 mm for all surfaces.

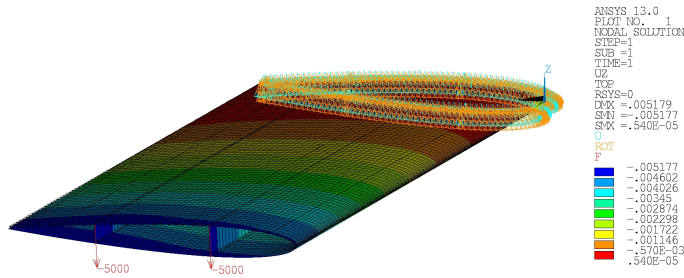


Figure 4: Static test using a wing with two nodal loads of 5000 N (mesh 128×80).

Table 1 contains a summary of the results. The displacement values are the maximum values for each case. A deviation of the results is calculated in relation to the finer mesh. A mesh having 32×20 panels proves to be a good approximation and still cheap in terms of computational cost.

Mesh	Displacement [mm]	Deviation
16×10	-5.387	4.1%
32×20	-5.219	0.8%
64×40	-5.186	0.2%
128×80	-5.177	0.0%

Table 1: Mesh study for the wing steady test.

3.1 Panel Method Validation

In order to get into the panel methods particularities, four computer programs were created: 2DS (two-dimensional steady), 2DU (two-dimensional unsteady), 3DS (three-dimensional steady) and 3DU (three-dimensional unsteady), all coded in MATLAB. The 2DS also uses constant doublets and sources but punctual singularities. It was validated using a *Kármán-Trefftz* airfoil, which has exact solution for potential flow. The 2DU was simply the same program with the time-stepping wake convection.

The 3DS, which is more important for this work, was validated with wind tunnel data and verified with a similar panel method program (called here 3DBalt) both documented in [7].

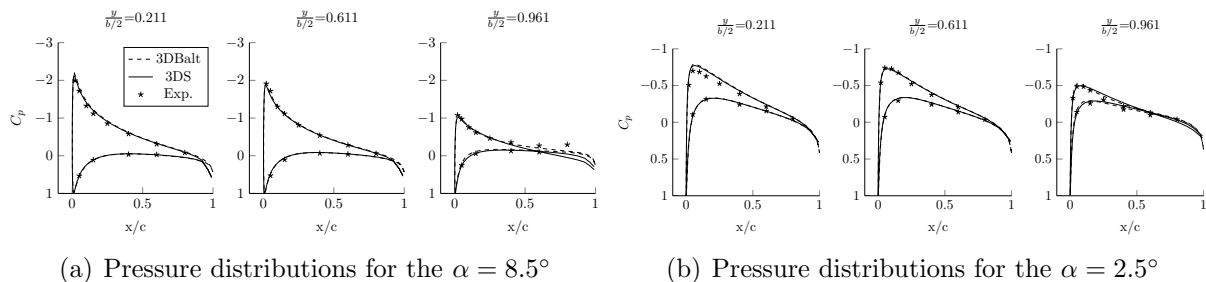


Figure 5: Comparison of pressure distributions for 3D steady case.

A wing with $R = 4$ and NACA 0015 airfoil is here applied. To have a fair comparison, a similar mesh of 64×32 panels is used with a cosine distribution on the spanwise direction. In Figure 5, 3DS shows a good approximation to the experimental results, even at the wing tip.

The consequence of the use of a linear Kutta condition can be clearly seen here, since 3DS shows an opened contour at the trailing edge. In contrast, with a converged solution using the iterative pressure Kutta condition, 3DBalt exhibits a fully closed curve.

Moreover, it is presented in Figure 6 a comparison of the non-dimensionalized circulation (or potential jump) of the wake, which shows good accordance of both panel methods. Herein, the cosine spanwise discretization makes the difference since the circulation changes closer to the wing tip, while it is almost constant close to the wing root. In this

case, a wing with $\mathcal{R} = 4$ and NACA 0010 airfoil was simulated.

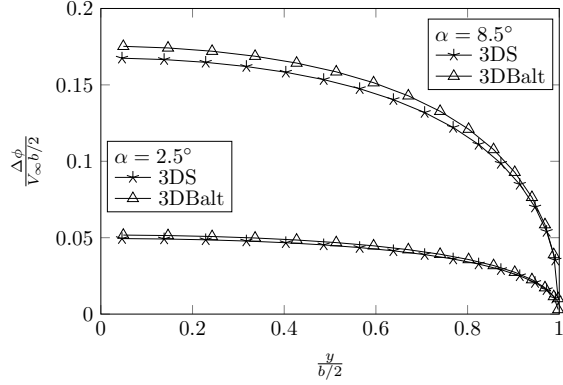


Figure 6: Comparison of the potential jumps along the span of the wing.

For the previous configuration, the lift and drag coefficients were evaluated at 6° angle of attack for different meshes and they are presented in Table 2.

Mesh	3DBalt		3DS	
	C_L	C_D	C_L	C_D
16×10	0.1082	0.0039	0.08842	0.0038
32×18	0.1024	0.0034	0.09376	0.0064
64×34	0.1002	0.0032	0.09572	0.0074
128×66	0.0993	0.0031	0.09632	0.0079

Table 2: 3D steady results comparison for different meshes.

The results are close between programs. However, while the refinement approximates 3DS to 3DBalt at the lift, it increases the difference in the induced drag predicted by 3DS as well.

3.2 Aeroelastic Design Framework

Next, both solvers were merged to perform the desired aeroelastic computations. The main script is coded in MATLAB, which calls APDL and reads its results in a very efficient fashion [10].

Figure 7 presents the main structure of the aeroelastic framework. The input box comprises all variables defined by the user before the computation. Organized in categories, they are:

1. **Fluid** - density, freestream velocity and angle of attack;
2. **Wing** - chord at wing root and tip, x and z coordinates of the point on the leading edge on the wing tip (defining the sweep and dihedral angles, respectively);

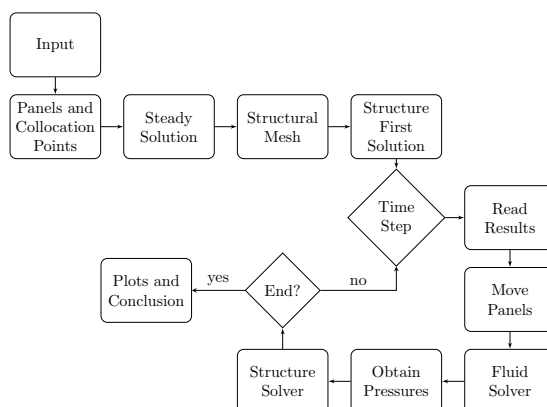


Figure 7: Flowchart illustrating the aeroelastic calculation process.

3. **Mesh** - file with the airfoil coordinates (the number of points dictates the number of chordwise panels), number of spanwise panels;
4. **Steady Wake** - initial steady wake angle and length;
5. **Structure** - spars location, material properties, thicknesses, presence of ribs;
6. **Time** - time step size, number of steps;
7. **Method** - Choice of coupling procedure (CSS or ISS) and time discretization method for the fluid domain (Backward Euler or Crank-Nicholson).

First of all, the wing panels and collocation points are stored in the respective variables and 3DS program is applied to introduce a steady solution for the specified angle of attack. This will produce the first set of loads.

Next, two lists are created in such a way that APDL is able to read it. One contains the nodes and their position and the other contains the elements and the information needed (nodes, material, section number, element type, and frame of reference). Those lists are saved in files and read in APDL. The difference of the first solution is that at the beginning the wing is at rest. In the subsequent ones, a set of initial conditions (velocity and displacement) is applied using the values of the last substep of the previous structure solution. This assures that one has continuity of the movement.

Figure 8 shows an example of a load case applied on a wing with $\alpha = 4^\circ$, obtained after the pre-processing stage. The elements of the structural mesh were created in such a way that the normals of the skin elements are pointing outwards by the right-hand rule.

After the initialization of the computation, the program enters in a cycle in the time domain. It begins by reading the file wrote by APDL and sorting the results, that contains the displacements and velocities for all nodes in all the time substeps computed in this visit.

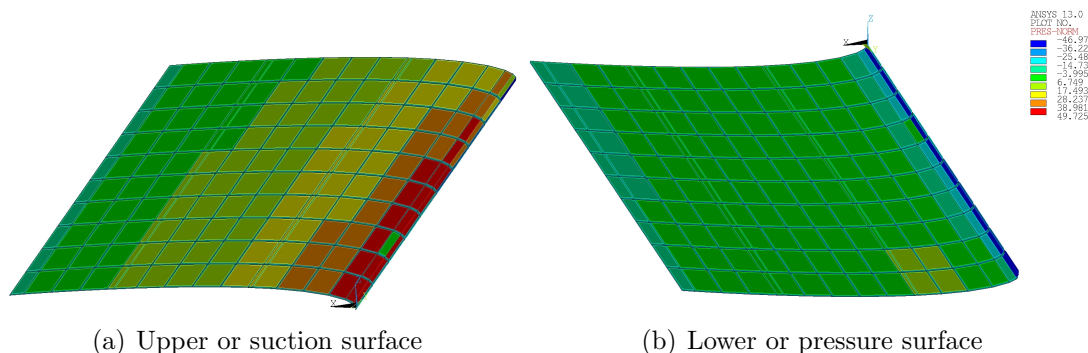


Figure 8: Example of a load case on an aircraft wing.

Then, the aerodynamic mesh is updated and introduced together with the previous wake positions and strengths into a fluid solver. The mentioned fluid solver is the 3DU program converted to a routine that receives the previous state as input and returns the velocity field in the next time step.

The pressure field is then computed using Equation (8) and the pressure vector is obtained from the dimensionalization of C_p with $\frac{\rho}{2}V_\infty^2$.

This cycle simply continues the solution until the desired time limit is reached. When the last cycle is completed, the last set of results is read. In this moment, some plots can be done to observe the behavior of the wing during the movement.

Figure 9 shows a possible post-processing manner which tracks the evolution of the wake during the whole calculation. This is the (X, Y, Z) frame and the wake is being convected with the flow velocity. The last panel row is wider because it represents the steady initial solution.

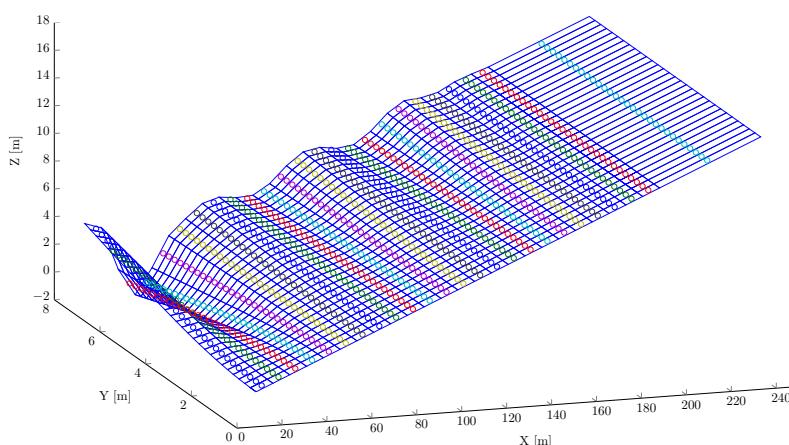


Figure 9: Example of the wake panels after 25 time steps (blue lines are the panel edges and colorful circles are the respective collocation points).

4 RESULTS

After having the framework finished, several initial tests were made to reduce the range of input options and have a set of results with physical sense and computationally cheap. One first study is here presented, which is called the *Reference Case* (RC). Later, several input parameters will be changed and their influence discussed, using the comparison with the RC.

4.1 Reference Case

The same input values used in the APDL static test from Section 3 are applied here, using a 64×30 mesh, $R = 15$, NACA 0010 airfoil, two spars at 30% and 70% chordwise location and the wing being rectangular with $c = 1$ m and no ribs. Moreover, the CSS procedure is applied using Backward Euler for the pressure time integration and Newmark in APDL for the structural time discretization.

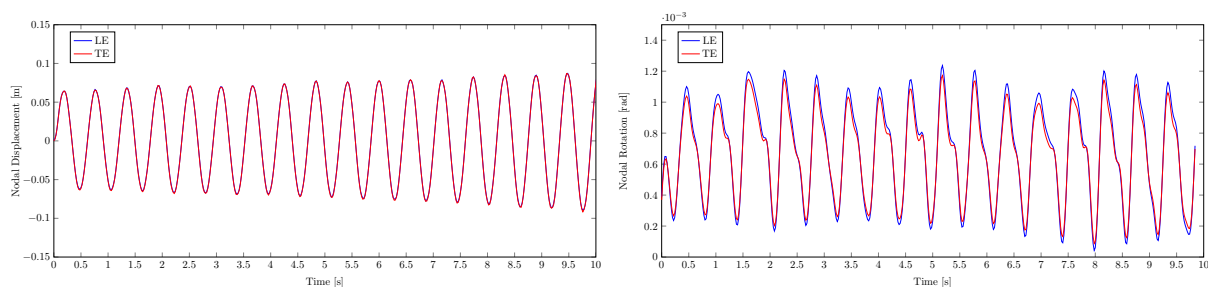
The fluid density is assumed to be $\rho = 1 \text{ kg/m}^3$ corresponding to an altitude of 1371 m at standard atmosphere conditions (considering a temperature offset of 20 °C), the angle of attack is $\alpha = 4^\circ$ and the fluid freestream velocity $V_\infty = 75 \text{ m/s}$. The initial wake angle is the angle of attack and its length is three time the wing span. The time step is set to 0.1 s.

To track the wing movement, the vertical displacement and the spanwise rotation of two nodes at the wing tip, one at the leading edge (LE) another at the trailing edge (TE), are plotted in Figure 10(a).

The nodal trajectory of both nodes is almost coincident so the torsion is very low. This is confirmed by Figure 10(b) that shows a maximal rotation of $2 \cdot 10^{-3} \text{ rad}$ which means roughly 0.1° . The rotational movement has the same period of the vertical displacement. When one is at the minimum displacement, it corresponds to the maximum rotation (positive rotation around Y is using the right-hand rule, from Z towards X axis, also called nose-up) and vice-versa. So, the torsional movement seems to be damping the bending movement. However, the increase of the wing maximal displacement shows clearly that this velocity is already higher than the flutter velocity.

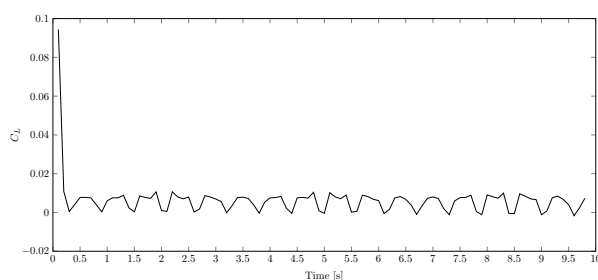
Using the peak values, the movement period and frequency are easily obtained. To obtain a consistent value, three values were used at the beginning, middle and end of the movement. The results are summarized in Table 3. Like it was expected, the frequency of the movement is nearly constant during all computation. If one counts the total number of peaks and divides by the respective time, the frequency obtained is 1.7 Hz, so that proves the constancy of the movement.

Figure 10(c) shows the evolution of the lift coefficient with the time. After the initial steady solution, the variation is not very significant, being however possible to see the oscillation caused by the wing movement, which varies with approximately the same frequency as the nodal displacement from Figure 10(a). Furthermore, lift positive peaks correspond to rotation positive peaks, which is physically correct.



(a) Vertical displacement of LE and TE wing tip nodes.

(b) Rotation of LE and TE wing tip nodes.



(c) Wing lift coefficient.

Figure 10: Aeroelastic reference results.

Time [s]	Frequency [Hz]
0.2	1.786
0.76	
8.9	1.724
9.48	
16.42	1.667
17.02	

Table 3: Period and frequency of the vertical movement of RC.

4.2 Freestream Velocity

The first parameter to study is the freestream velocity. Three velocities smaller than the RC value are tested, in particular 10 m/s , 40 m/s and 60 m/s . Figures 11(a) and 11(b) show the LE node behavior. The TE was suppressed because its movement is almost coincident with the LE.

The graph for $V_\infty = 60 \text{ m/s}$ is still smoothly divergent, while at 40 m/s has practically zero damping. So it is concluded that the flutter velocity is around 40 m/s . At 10 m/s , the wing has no perceived oscillation.

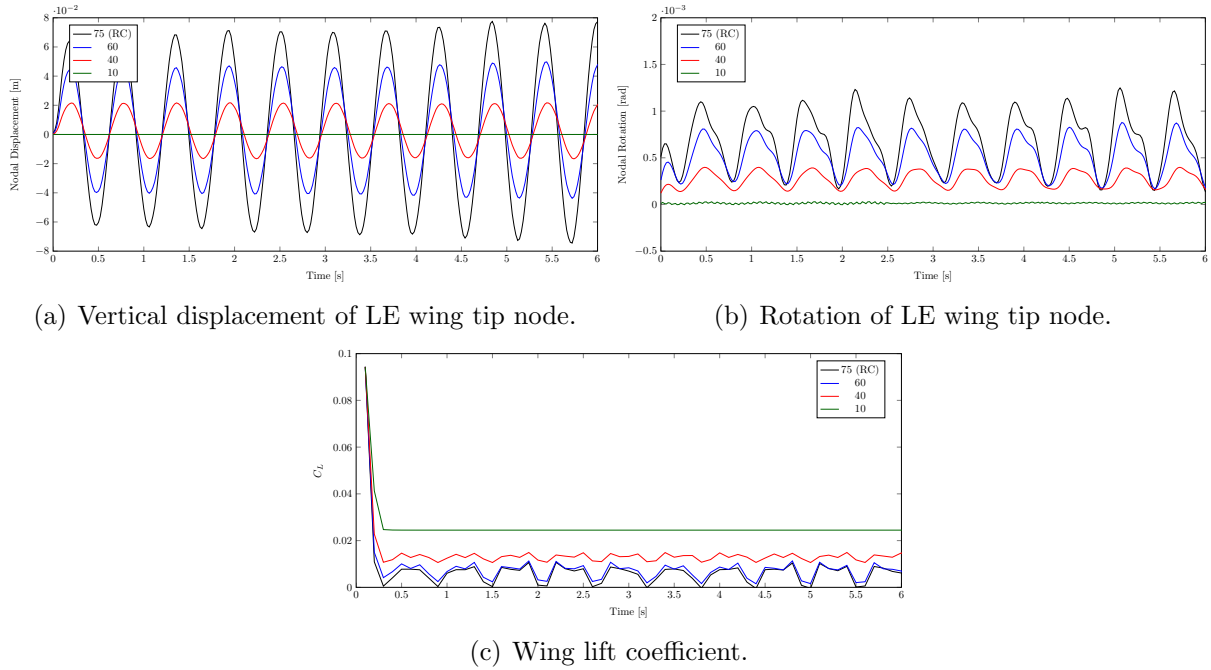


Figure 11: Influence of the freestream velocity [m/s] in the aeroelastic wing behavior.

In Figures 11(a) and 11(b), it is possible to see the bending-torsion coupling, since both movements have the same frequency, however opposite phase (i.e. 180 degrees difference). Watching also Figure 11(c), one can confirm that the positive rotation is a nose-up position, since the lift coefficient has also a maximum. Moreover, the lift has the same frequency of the rotational and bending movements.

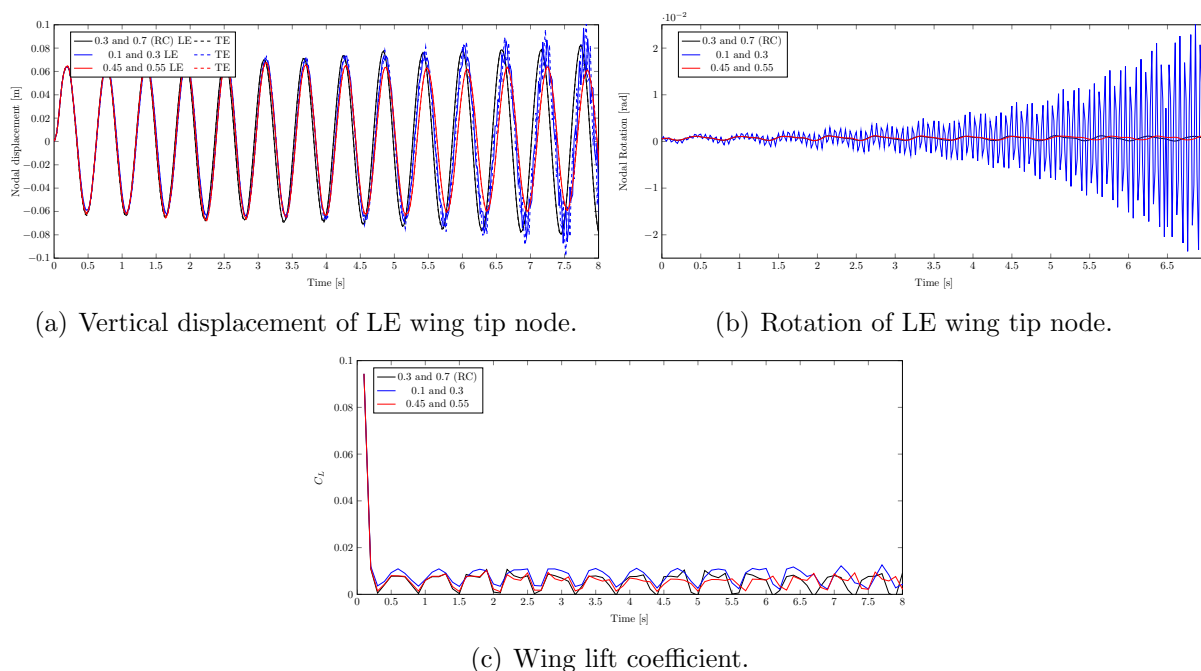
As it is expected, the frequency of the movement does not change with the freestream velocity. As it will be seen later, other parameters will have this effect.

4.3 Spar Location

The next test is made changing the location of the two wing spars. As it will be seen, by moving the spars in the chordwise direction towards one of the edges, one is changing the wing torsional stiffness, maintaining the bending movement frequency very similar.

Three computations were done with the spars at: 70% and 90% chord, which means close to the trailing edge; 10% and 30%, close to the LE; and 45% and 55%, closer to each other than the RC (30% and 70% chord).

In the first case, the wing movement is largely divergent and the vertical displacement reaches the order of meters in a few seconds, so it will not be plotted here. This result was expected since, in practice, what was done was to move away the twist center from the aerodynamic center. This causes torsional divergence [8] and, consequently, also bending divergence.



(a) Vertical displacement of LE wing tip node.

(b) Rotation of LE wing tip node.

(c) Wing lift coefficient.

Figure 12: Influence of the spars location (measured in chords) in the aeroelastic wing behavior.

Figure 12 shows the results for the other cases compared with the RC. Figure 12(a) confirms that the bending frequency was not affected. However, by placing the spars closer to each other at the wing center, the flutter velocity increased and the nodal maximum vertical displacement is decreasing very slowly in this case.

The lift coefficient is also not significantly affected, maintaining also the frequency accordingly to the displacement.

The big difference is the torsional movement when the spars are pushed towards the LE, which places the center of twist ahead of the aerodynamic center. As it can be seen in Figures 12(a) and 12(b), the bending movement is still similar but a torsional divergence with higher frequency appears.

4.4 Skin Density

The next two parameters to change are related to material constants. The material changes in the spars did not affect significantly the wing dynamic behavior, so only the changes in the skin are presented here.

Herein, the influence of the density is investigated, which will have influence on the structural mass matrix M . Equation (1) shows that M influences the inertial forces, since it is multiplied by the acceleration vector $\ddot{\vec{u}}$. So, the higher the density, the higher the inertial forces.

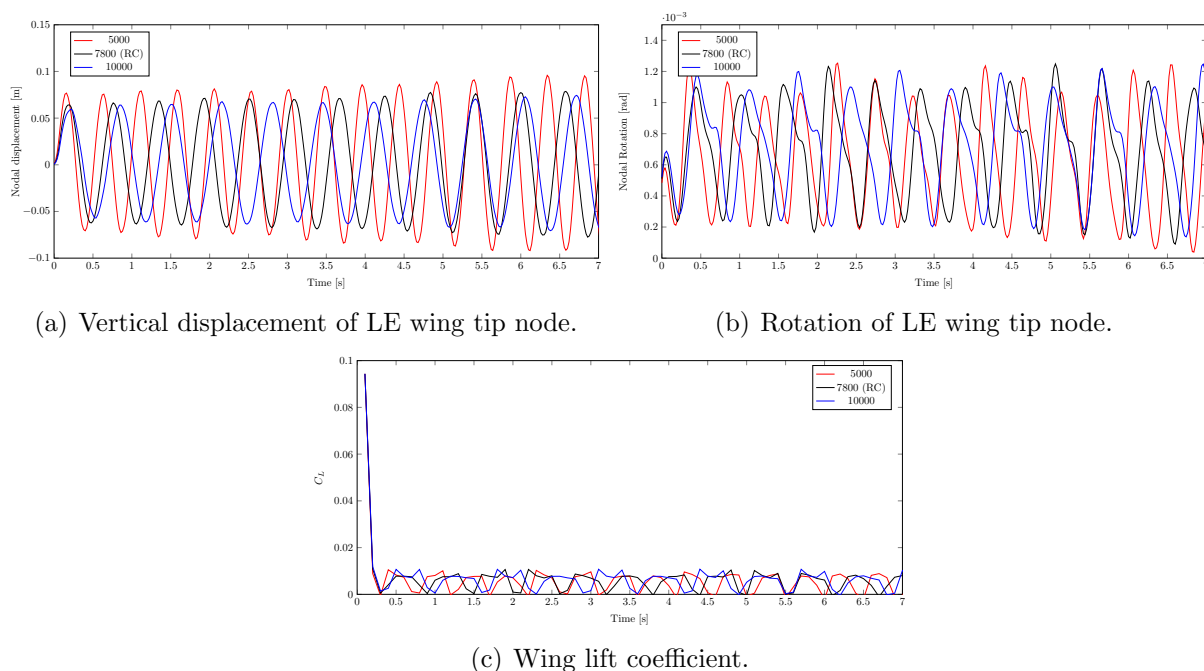


Figure 13: Influence of the skin density $[\text{kg}/\text{m}^3]$ in the aeroelastic wing behavior.

In Figure 13(a), one can immediately see that the density influences mainly the frequency of the vertical movement. The higher the material density, the smaller the flutter frequency, as expected from basic principles of mechanical vibrations ($f \propto \sqrt{k/m}$). Table 4 summarizes the frequency calculation for three computations, corresponding to the RC and a less and a more dense material.

Density $[\text{kg}/\text{m}^3]$	Frequency [Hz]
5000	2.10
7800	1.72
10000	1.54

Table 4: Frequency of the vertical movement for changing material density.

Figure 13(a) also shows that reducing density also helps the wing to diverge, since the peak values increase in comparison with the RC. In reverse, the heavier wing has more inertia causing the amplitude of the oscillations to be smaller.

Figures 13(b) and 13(c) basically show accordance to 13(a) in terms of the frequency, like it was expected.

4.5 Skin Young Modulus

Next, the influence of the elasticity or Young modulus E will be tested. Increasing E makes the material more stiff, while decreasing makes it more elastic. Having the reference value of 200 GPa , two more computations were made for 100 and 300 GPa .

The results are clear in Figure 14. As soon as one decreases the Young modulus, both bending and torsion amplitudes will increase, likewise the period. In this specific case, the increase to 300 GPa also transforms the movement to convergent, since the amplitude is decreasing with the time. These results corroborate once again the principles of mechanical vibrations since frequency f is proportional to stiffness k as $f \propto \sqrt{(k/m)}$. The lift coefficient does not suffer a significant change, besides the frequency which is in accordance with Figures 14(a) and 14(b).

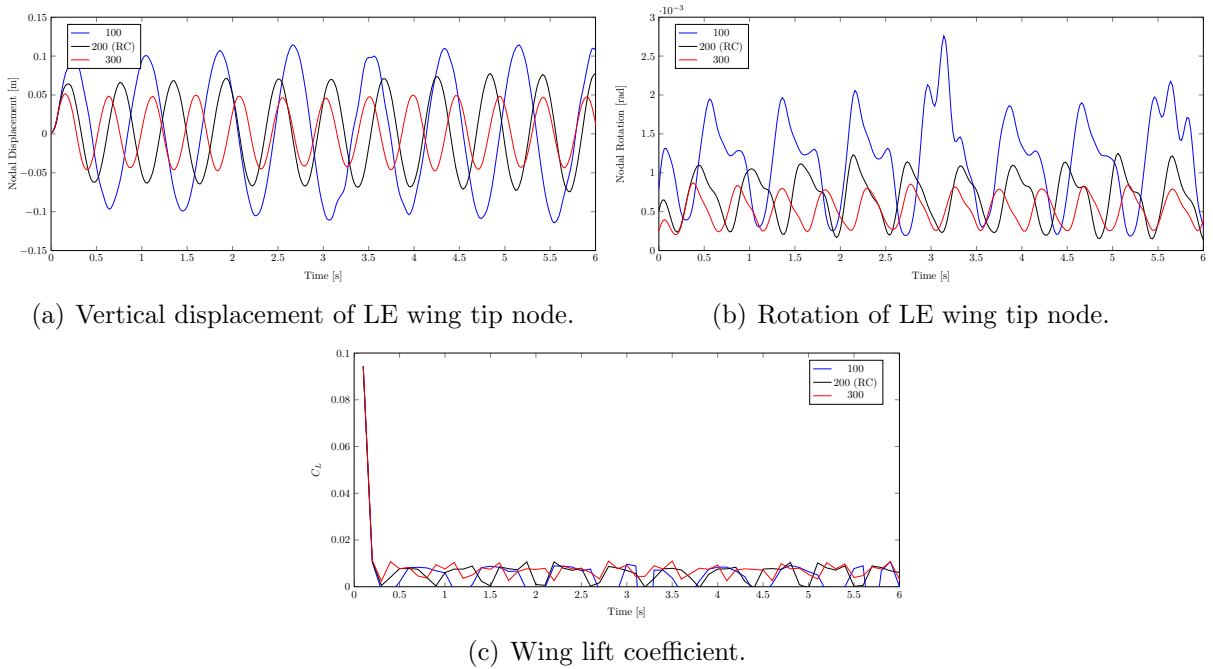


Figure 14: Influence of the skin Young modulus [GPa] in the aeroelastic wing behavior.

5 CONCLUSIONS

An aeroelastic design framework was presented for the study of aircraft wings. It is composed by three main parts: the structure solver APDL, the fluid solver a panel method coded in MATLAB and a coupling procedure also in MATLAB which controls the other two parts.

The fluid solver was fully developed in MATLAB, going from the steady two-dimensional to the unsteady three dimensional problem, being the two-dimensional case validated with

exact results from the potential theory and the three-dimensional validated with wind tunnel tests. Furthermore, the results were also compared with another panel method program presented in [7] and with XFOIL.

The mesh nodes and elements, the material constants, the section types and thickness, the loads and the initial conditions are saved to files by MATLAB and then read from APDL, which, in turn, writes the nodal displacements, velocities and rotations to another files. This method proved to be very efficient and reliable.

The FSI normally generates some issues like the transfer of loads and displacements, the frame of reference and the added mass. The first two were very simplified, since the fluid solver used made it possible to use the same grid in both domains, having only left the Load Lumping issue, which was proved to be accurate. The latter just influences cases when the fluid and structure densities are comparable (for instance blood flows inside veins), which is not the case in aircraft applications.

The aeroelastic framework created starts with a fluid steady solution for the values input by the user. Then, it generates the structural mesh which remains the same during all the computation. After the first structural solution, a time cycle starts performing a defined number of cycles with the same time step for both fluid and structure solver. The latter has however the possibility to have substeps to track the body movement more precisely. In dynamic aeroelasticity, it is usual to calculate the flutter velocity. Therefore that was the first parameter to vary and the results show that it is possible to calculate an approximate flutter velocity for an aircraft wing. The other tests showed that the spar position changes the wing center of twist, the sweep angle changes the coupling between the bending and torsion movements, the skin density influences the inertial forces and consequently the period and amplitude of the bending movements, as well as the Young modulus which influences the material stiffness or elasticity.

Future work will be pursued in shape or topology optimization using the aeroelastic analysis framework here developed and presented. Tackling problems of flutter speed maximization of an aircraft wing with constraints in weight is something of utmost importance in very high performance aircrafts.

ACKNOWLEDGMENTS

We want to express our gratitude to Professor Luís Eça for his pertinent and helpful advices and Doctor João Baltazar for kindly providing his PhD thesis and results used in the validation of the aerodynamic calculations.

REFERENCES

- [1] R. L. Bisplinghoff, H. Ashley and R. L. Halfman, *Aeroelasticity*, Dover Publications, Inc., First ed. (1996).
- [2] E. H. Hirschel, H. Prem and G. Madelung, *Aeronautical Research in Germany From Lilienthal until Today*, Springer-Verlag, First ed. (2004).

- [3] ANSYS, Inc., *Theory Reference for the Mechanical APDL and Mechanical Applications*, Release 13.0 (2010).
- [4] C. Hirsch, *Numerical Computation of Internal and External Flows*, Vol. I, Butterworth-Heinemann, Second ed. (2007).
- [5] J. Katz and A. Plotkin, *Low-Speed Aerodynamics*, Cambridge University Press, Cambridge Aerospace Series N. 13, Second ed. (2001).
- [6] C. Farhat and M. Lesoinne, *Two efficient staggered algorithms for the serial and parallel solution of three-dimensional nonlinear transient aeroelastic problems*, Computer Methods in Applied Mechanics and Engineering, Vol. **182**, N. 3-4, pp. 499-515, (2000).
- [7] J. Baltazar, *On the modelling of the potential flow about wings and marine propellers using a boundary element method*, Instituto Superior Técnico (IST), PhD dissertation (2008).
- [8] T. H. G. Megson, *Aircraft Structures for Engineering Students*, Butterworth-Heinemann, Fourth ed. (2007).
- [9] Brian Maskew, *Program VSAERO Theory Document*, NASA (1987), Contractor Report n. 4023.
- [10] MathWorks, *Use Matlab Editor to Write and Run Ansys Program*, March 2011, <http://www.mathworks.com/matlabcentral/fileexchange/30887-use-matlab-editor-to-write-and-run-ansys-program>.
- [11] A. R. Collar, *The First Fifty Years of Aeroelasticity*, Aerospace, Vol. 5, N. 2, pp. 12-20, (1978).
- [12] Ramji Kamakoti and Wei Shyy, *Fluid-structure interaction for aeroelastic applications*, Progress in Aerospace Sciences, Vol. 40, N. 8, pp. 535 - 558, (2004).